

PAPER

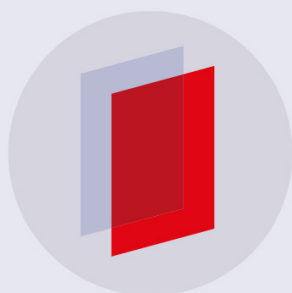
Carbon nanotube alignment driven rapid actuations

To cite this article: Yu-Hsien Lin *et al* 2013 *Nanotechnology* **24** 465501

View the [article online](#) for updates and enhancements.

Related content

- [Establishing Ohmic contacts for in situ current–voltage characteristic measurements on aCNT inside the SEM](#)
Qing Chen, Sheng Wang and Lian-Mao Peng
- [A study on the mechanical and electrical reliability of individual carbon nanotube fieldemission cathodes](#)
Bryan P Ribaya, Joseph Leung, Philip Brown *et al.*
- [An exceptional bimorph effect and a low quality factor from carbon nanotube–polymercomposites](#)
Wen-Kuang Hsu, Huai-Yuan Chu, Ting-Hsien Chen *et al.*



IOP | ebooks™

Bringing you innovative digital publishing with leading voices to create your essential collection of books in STEM research.

Start exploring the collection - download the first chapter of every title for free.

Carbon nanotube alignment driven rapid actuations

Yu-Hsien Lin¹, Hsin-Jung Tsai¹, Han-Chen Chang¹, Wen-Yi Lin¹,
Wei-Leun Fang² and Wen-Kuang Hsu¹

¹ Department of Materials Science and Engineering, National TsingHua University, HsinChu, 30013, Taiwan

² Department of Power Mechanical Engineering, National TsingHua University, HsinChu, 30013, Taiwan

E-mail: wkhsu@mx.nthu.edu.tw

Received 10 June 2013, in final form 2 September 2013

Published 24 October 2013

Online at stacks.iop.org/Nano/24/465501

Abstract

Suspended micro-beams made from aligned carbon nanotubes and parylene deflect reversibly in an ac field and the deflection rate is three orders of magnitude greater than those for existing devices. The direction of beam deflection is determined by the area moment of inertia and the actuation mechanism involves rapid accumulation of charges at tube surfaces, the creation of Coulomb repulsive forces between tubes, beam dilation and the formation of compressive stresses at beam ends. Tube alignment plays a crucial role in the first step as is verified by experimental data and calculation.

 Online supplementary data available from stacks.iop.org/Nano/24/465501/mmedia

(Some figures may appear in colour only in the online journal)

1. Introduction

Carbon nanotubes (CNTs) are one-dimensional conductors made of rounded graphene sheets and do not suffer from the Peierls distortion at low temperature [1]. Upon bending, stresses are dispersed through rigid networks and s-p electrons re-hybridize to prevent bond dissociations at bends [2]. When submerged in electrolyte, double layer charging causes a breakdown of hexagonal symmetry and tubes actuate to release stresses—the displacement (D_m) being estimated to be tens of microns [3, 4]. Study reveals that strain creation is of quantum chemical origin and structural contraction and expansion (bimorph effect, BE) due to doping take place at a potential as low as 0.2–0.5 V [3, 4]. Intercalations of ions in CNT yarns also produce actuations and the BE due to the Coulomb forces created by tensile and torsional strains [5]. Compared with the conventional micro-electromechanical system (MEMS), the electrochemically driven D_m is much smaller and actuator fabrication is time-consuming. Recent study has focused on devices made of CNTs and polymers and the conversion of electrical energy into mechanical movements is through a

thermal bimorph effect (TBE). Reports indicate that thermal stresses can be optically or electrically created: the former employs an intensity light to generate photocurrent in CNTs and stresses then form as a result of joule heating at intertube barriers [6]. TBE-driven actuators however can barely operate at a high frequency regime (> 10 Hz) and deflection rate (V_D) has been measured to be as low as $0.1 \mu\text{m s}^{-1}$ [7, 8]. In this work, arrays of aligned multi-walled CNTs (MWCNTs) are filled with polymer and the resultant composites are shaped into suspended micro-beams. Upon application of alternating current (ac), beams deflect reversibly and V_D exceeds $100 \mu\text{m s}^{-1}$. Actuations are of electromechanical origin and involve four consecutive steps, including rapid accumulation of charges at tube-polymer interfaces, creation of Coulomb repulsive forces (F_C) between tubes, F_C induced beam dilation, and the formation of compressive stresses (σ) at beam ends. CNT alignment plays a crucial factor in creating F_C and the F_C - σ driven mechanism is characterized by low joule heating, a linear plot of beam strain (ϵ) versus applied voltage (V) and synchronization of deflection frequency (f_D) with applied frequency (f).

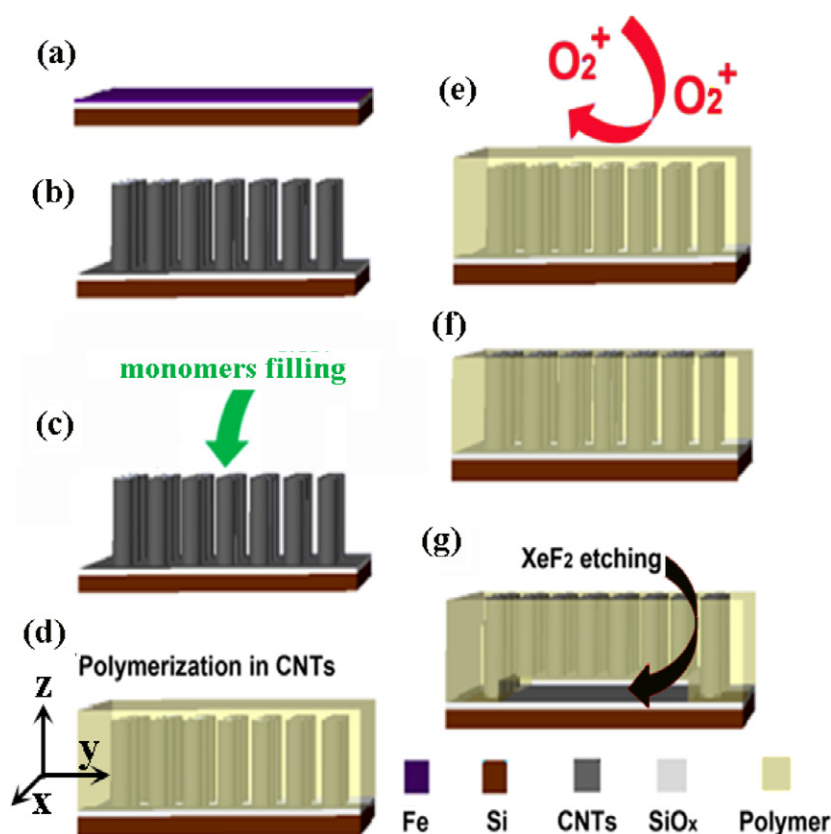


Figure 1. (a) Sputter-coating and photolithographic defining of catalytic Fe layer on a SiO₂/Si substrate, (b) growth of aligned MWCNTs, (c) the filling of parylene monomers into the array, (d) parylene polymerization in MWCNT array, (e) the O₂⁺ plasma etching of composite surfaces, (f) etched composite beam and (g) the partial etching of substrate by XeF₂ technique.

2. Experimental details and discussion

CNT actuators are made according to the following procedure. First, a polysilicon wafer is coated with a thin film of Fe (5 nm) as catalytic agent and the coated substrate is placed in an alumina furnace heated at 850 °C (figure 1(a)). A mixture of acetylene/N₂/H₂ (2:7:1, 200 sccm) is introduced into the furnace and pyrolysis is carried out for 10 min. Scanning electron microscopy confirms the growth of MWCNTs on the wafer and the tube length lies in the range 98–100 μm (figure 1(b)) [7]. Second, the poly-para-xylylene dimers (tradename: parylene, 100 mg) are placed in a heating chamber connected to the furnace and are subsequently vaporized at 150 °C. Methylene gas (150 sccm) is introduced into the chamber to mix with the parylene vapor and the chamber temperature is further raised to 680 °C to decompose the gas mixture into stable monomeric diradical para-xylylene. Third, monomers are redirected from the chamber to the furnace; this initiates polymerization in the CNTs and produces a long-fiber composite with density of 1.35–1.39 g cm⁻³ (figures 1(c) and (d)). Fourth, the surface polymer is removed by O₂⁺ plasma (figures 1(e) and (f)) and the exposed tubes are verified by field emission and electrical measurements as follows. A phosphor coated indium–tin–oxide glass is used as electron collector and the anode and sample surface are spaced 300 μm apart. The emission chamber is evacuated to 10⁻⁶ Torr and

emission current (E_C) is recorded with an IEEE-488 interface controlled Keithley-237 power supply. For two-terminal measurements, tungsten tips are placed onto etched surfaces and current–voltage (I – V) profiles are recorded at bias voltage of 0.1–1.5 V. Fifth, a mask-assisted gas-phase XeF₂ technique is used to etch the beam substrate and the suspended structure is verified with an optical microscope (figure 1(g)) [7]. Two suspended micro-beams, defined as devices A (1160 × 20 × 98 μm³) and B (1160 × 80 × 98 μm³), are constructed (circles, figures 2(a) and (b), (c)) and actuations are driven with a component analyzer in ac mode. The D_m is measured with a laser micrometer (±0.1 μm) and f_D is recorded with an optical microscope (×1000) equipped with a charge coupled device camera (×2). The video footage is available in the supporting information (SI available at stacks.iop.org/Nano/24/465501/mmedia). The mechanical strength of the actuators is measured by commercial thin-film indentation using magnetic coils as the force induction (MTS, Nano-indenter, resolution ±1 nN), and displacement magnitude is recorded with a capacitive sensor. A triangular pyramid tip is employed (Berkovich indenter) and tip displacement *versus* load is recorded *in situ*.

The pristine arrays of aligned MWCNTs are of porous structure and pore volume lies in the range 0.209–0.215 cm³ g⁻¹ according to Brunauer–Emmett–Teller measurement (figures 3(a)–(c)). Porosity however decreases as polymer is added and reduction reaches 75–85%

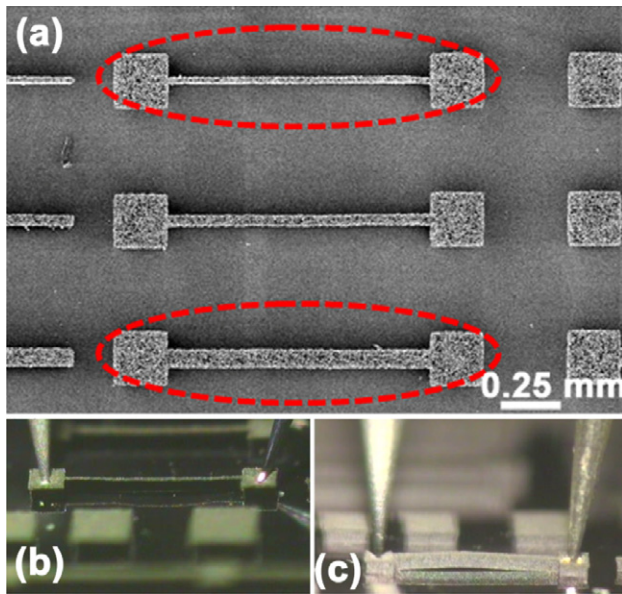


Figure 2. (a) SEM images of polymer-filled MWCNT arrays, and (b) optical images of devices A and (c) B. Red circles: top views of devices A and B.

(figures 3(d)–(f)). Polymerization also causes a widening of the array dimension by 1% and tube alignment morphology becomes obscure (figures 3(b) and (e)); the latter is further supported by immeasurable (i) surface resistivity and (ii) E_C . Composites become conductive as surface polymers are etched and the exposed tubes create distinguishable E_C at 180–200 V (figure 4(a)). The E_C then increases rapidly at 210–220 V and the threshold field ($\approx 10 \text{ mA cm}^{-2}$) is estimated to be $3 \text{ V } \mu\text{m}^{-1}$, comparable with those for existing CNTs-based emitters [9]. It is noteworthy for nanotubes arranged in a chaotic fashion that emission performance is always challenged by a screening effect and a thermionic process; the former arises from the space charge between

tubes and results in a low E_C [9]. The latter is owing to charge transfer induced thermalization at intertube contacts and is characterized by the non-linear Fowler–Nordheim (F–N) plot [10]. The nanotubes here are embedded in polymer and electron emission takes place only at exposed tips, accounting for significant E_C and a linear F–N plot (upper and lower insets, figure 4(a)) [11]. Additional evidence in support of tip emission promoted E_C comes from the low resistivity data. Figure 4(b) shows linear I – V profiles obtained from various regions of an interconnected array (inset) and average resistivity is $2 \times 10^{-5} \Omega \text{ m}$ —a value which is one order of magnitude lower than that on composites loaded with dispersed tubes [10].

CNT–polymer composites, made by mechanical blending between nanotubes and polymers, or by polymerization in the presence of nanotubes, are constantly challenged by phase separation and interfacial weakness. The former reduces packing efficiency and facilitates crack propagation. The latter shortens the load carrying length and leads to inefficient load transfer [12]. Aligned CNT-reinforced composites possess a maximized packing efficiency and the load carrying length is about the same length as the nanotubes [13]. Accordingly, beams produced here can be considered as an elastic continuum and a relative ease of bending is expected to lie on the axis with a lower area moment of inertia (I) or bending moment (M_B) [14, 15]. Laser micrometer reveals the ratio of beam width (w) to height (h) to be 0.2 and 0.81 for devices A and B; $w/h < 1$ indicates the presence of lower M_B at the x -axis (inset, figure 5(a)). Video footage confirms that device A truly deflects along the x -axis and f_D synchronizes with f (supporting information, SI available at stacks.iop.org/Nano/24/465501/mmedia). Figure 5(a) plots V versus ε [$= ((L_0 - L_S)/L_0) \times 100\%$], where L_0 and L_S denote the beam length at $V = 0$ and $V \neq 0$. At 1.5 V, ε is 0.01% and increases to 0.035% at 2.5 V (figure 5(a)). The ε continues to increase and reaches 0.1% at 4 V, a value which is twice that of conventional MEMS devices operating at a similar voltage [13]. The joule

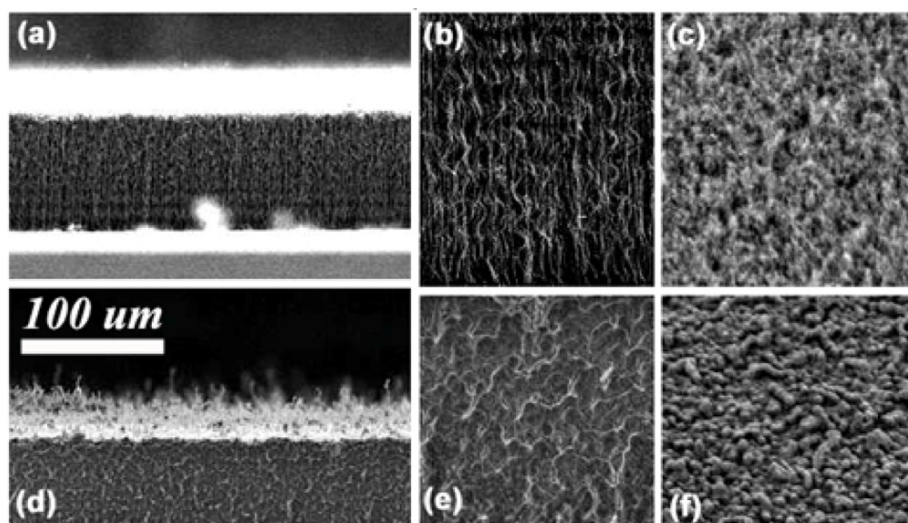


Figure 3. SEM images of (a) as-grown MWCNT array, (b) side-view and (c) top-view. SEM images of (d) polymer-filled MWCNT array, (e) side-view and (f) top-view.

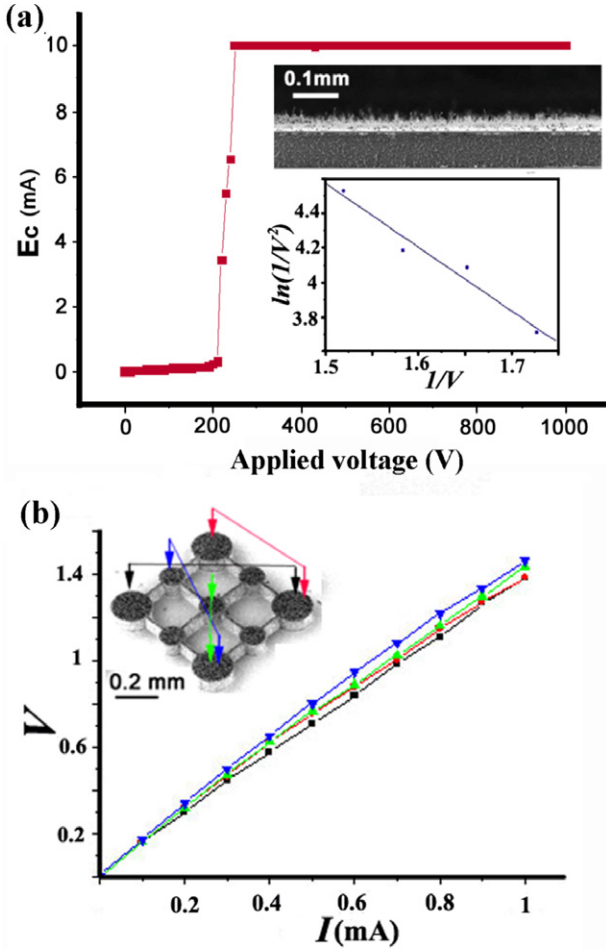


Figure 4. (a) The field emission profile of an O_2^+ -plasma etched CNT-parylene composite beam. Inset: enhanced image of emitter surface (top) and F-N plot (lower), and (b) The I - V profiles of interconnected arrays. Inset: arrows denote probe locations (colors).

heating however is low and beam temperature, as revealed by infrared thermometer, only rises by $1-2 \pm 0.5^\circ\text{C}$ at 5 V and by $2-4 \pm 0.5^\circ\text{C}$ at 10 V, ruling out TBE-driven actuation. Electromechanically driven actuations are also supported by fact that $\varepsilon \neq 0$ only takes place at $V \neq 0$ whereas TBE-driven actuations, due to residual heat, often continue at $V = 0$ [13].

In the light of the observations above we believe that beam deflection originates from charge accumulation at the tube surfaces and proceeds through four consecutive steps: (i) charging created F_C between tubes, (ii) beam dilation along the y -axis (figure 5(b)), (iii) σ formation at beam ends, and (iv) beam buckling. Item (i) has been verified as a result of differentiated dielectric constant at tube/polymers interfaces [2] and (ii) is due to F_C formation between tubes. Dilation however is inhibited by the end-fixed structure so the beam buckles (iii)-(iv) and deflects along the x -axis for $w/h < 1$ and along the z -axis for $w/h > 1$ (figure 5(c)). According to the Rayleigh instability model the intertube cohesive energy is the sum of F_C acting on individual tubes and is equivalent to CNT resilience energy ($E_r \approx 2F_C$) (insets, figure 5(d)) [14, 15]. Based on reported data the E_r is taken to be 1.1×10^{-14} J and the electrical potential (U)

between tubes can then be calculated according to [14]

$$U = \sqrt{\frac{-2E_r \ln\left(\sqrt{\left(\frac{l}{r_0}\right)^2 + 1} - \frac{l}{r_0}\right)}{\pi \varepsilon_0 l}},$$

where r_0 is intertube separation ($=0.2 \mu\text{m}$), l is $49 \mu\text{m}$ and ε_0 is vacuum permittivity ($=8.854 \times 10^{-12} \text{ F m}^{-1}$). Insertion of the cited numbers into the equation gives $U = 7.02 \text{ V}$ and linear charge density ($q = 2E_r/1U$) on individual CNTs appears to be $0.196e^{-1} \text{ nm}^{-1}$, corresponding to $1.225 \times 10^{-2}e^{-1}/\text{atom}$. This value is slightly greater than the energy required for nanotube segregation from a bundle ($0.9 \times 10^{-2}e^{-1}$), supporting F_C creation between tubes and beam dilation [14, 16]. In practice, F_C emerges mostly at intertube junctions and can be calculated by the Coulomb force equation $F_C = CV^2/r_0$ where C is capacitance. Figure 5(d) plots ε versus V^2 and the linear profile again verifies the F_C - σ driven actuations [16].

We now calculate M_B based on the equation $M_B = EI/\delta$ where I and the radius of curvature (δ) are measured to be $6.53 \times 10^{-12} \text{ cm}^4$ and 0.84 cm for device A and $6.27 \times 10^{-10} \text{ cm}^4$ and 1.01 cm^4 for device B. Young's modulus (E) is set as $3.06 \times 10^4 \text{ kg cm}^{-2}$ according to reported data [13]. Insertion of the cited values into the equation gives $M_B = 2.38 \times 10^{-7}$ and $4.74 \times 10^{-5} \text{ kg cm}$ for devices A and B, and the dilation σ created at beam ends, according to the equation $\sigma = M_B w/2I$, is 3.57 and 711 MPa , respectively. Compared with MEMS devices the M_B obtained here is much lower, which is attributed to the polymer endowed flexibility. Figure 6 shows an indented structure at the beam surface: first, a rapid resilience occurs and a diamond-shaped crater rapidly vanishes; second, polymer is slightly ruptured by tip-impact and resilience takes place mainly at pyramid faces, thus forming a punctured hole (top insets). Figure 7(a) plots D_m versus V ; data points have been calibrated with Photoshop software at $\pm 0.1 \mu\text{m}$ resolution. On the first run, D_m is $5 \mu\text{m}$ at 3.5 V and increases to $30 \mu\text{m}$ at 9 V , the average being $4.5 \mu\text{m V}^{-1}$. The D_m profiles become stabilized at the second to fourth run and the mean value of D_m slightly decreases by $0.4 \mu\text{m V}^{-1}$, possibly owing to charge redistribution at tube surfaces [17]. Figure 7(b) shows time-evolved f_D profiles—measurements start with $f = 2 \text{ Hz}$. At $t = 0-11 \text{ s}$, the beam buckles and unbuckles twice ($f_D = 2$); the time frame ($T_{\text{frame}} = \text{buckled} \rightarrow \text{unbuckled}$) for a full cycle of beam deflection is 0.5 s according to the equation $T_{\text{frame}} = 1/f_D$. The f is tuned to 4 Hz at $t = 12 \text{ s}$ and the f_D and T_{frame} change to 4 and 0.25 s . The f_D - f synchronization is also supported by the reduced spacing between D_m peaks at $t = 12 \text{ s}$ (inset, figure 7(b)), again ruling out the TBE mechanism. D_m however does not change with f tuning and is measured to be $20 \pm 0.3 \mu\text{m}$ at $t = 12, 13,$ and 18 s . We then calculate V_D according to T_{frame} and find $V_D = 400 \mu\text{m s}^{-1}$ at $f = 10 \text{ Hz}$ and $800 \mu\text{m s}^{-1}$ at $f = 13 \text{ s}$, a value which is three orders of magnitude greater than that of TBE-driven actuators [18]. Device B also buckles reversibly in an ac field whereas the beam deflects along the z -axis, in contradiction to the $w/h < 1$ criterion (SI). Careful examination reveals that

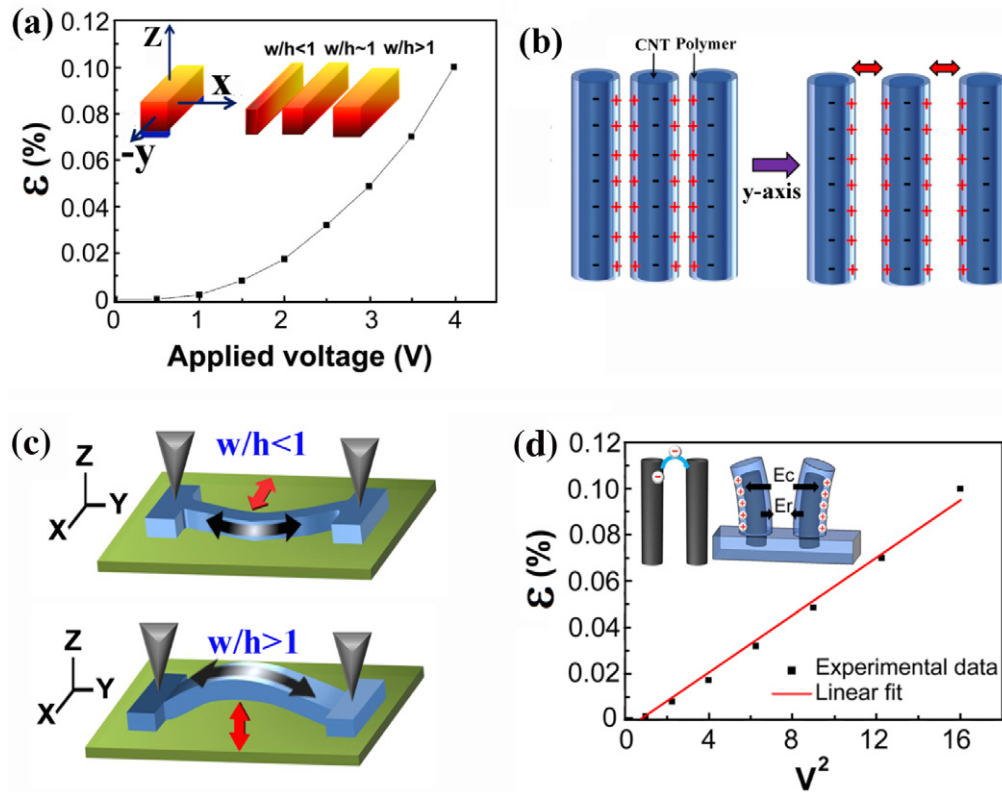


Figure 5. (a) The ε - V plot obtained from device A. Inset: the w/h controlled direction of beam deflections, (b) F_C creation between tubes and beam dilation along the y -axis, (c) the direction of beam deflection for $w/h < 1$ (top) and $w/h > 1$ (lower), (d) the ε - V^2 plot of device A. Inset: the Rayleigh instability model.

the beam bends slightly upward before electrical application and arching possibly originates from probe created stresses at the beam ends (figure 2(c)). In this case, δ at the z -axis increases and M_B is reduced, resulting in z -axial deflection. The F_C - σ mechanism however remains in device B and is supported by f_D - f synchronization (SI).

The question remains as to why TBE is absent in the current study. The fact is that the actuations originate from F_C creation between the tubes and the beam only dilates as F_C exceeds E_r (inset, figure 5(d)). In this respect, tube alignment plays a crucial role in promoting q and is supported as follows. First, alignment yields a greater interface and q . Second, beams made from dispersed MWCNTs and polymer do not actuate with the F_C - σ mechanism and deflections are driven by the TBE mechanism (figures 8(a)-(h)). At 1–2 V, beam deflection is small and the optical micrometer gives $D_m < 1 \mu\text{m}$ (figures 8(a)-(d)). Large deflections then take place at >2.5 V and D_m is measured to be $15 \mu\text{m}$ at 3 V and $20 \mu\text{m}$ at 3.5 V (figures 8(e)-(g)). Embedded CNTs become resistive at 4 V and joule heating induces buckling distortion (figure 8(h)). The buckled beam however does not unbuckle at $V = 0$ and V_D is as low as $5 \mu\text{m s}^{-1}$, indicative of the TBE-driven mechanism.

3. Conclusion

Vapor-phase polymerization of parylene in aligned MWCNTs produces a long-fiber composite system and good

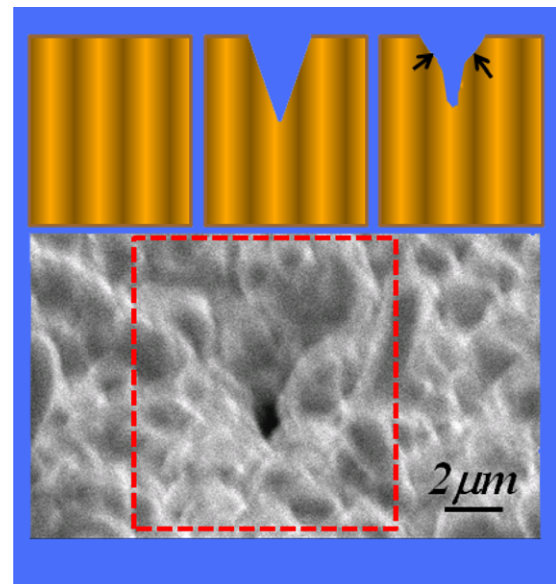


Figure 6. Indented region (square) and impacted structure. Inset: formation of a punctured hole.

conductivity is evidenced by linear I - V plots and high E_C . When composites are shaped into suspended beams reversible buckling occurs upon ac voltage application and f_D synchronizes with f . Actuations are of electromechanical origin and involve (i) charge accumulation at tube-polymer

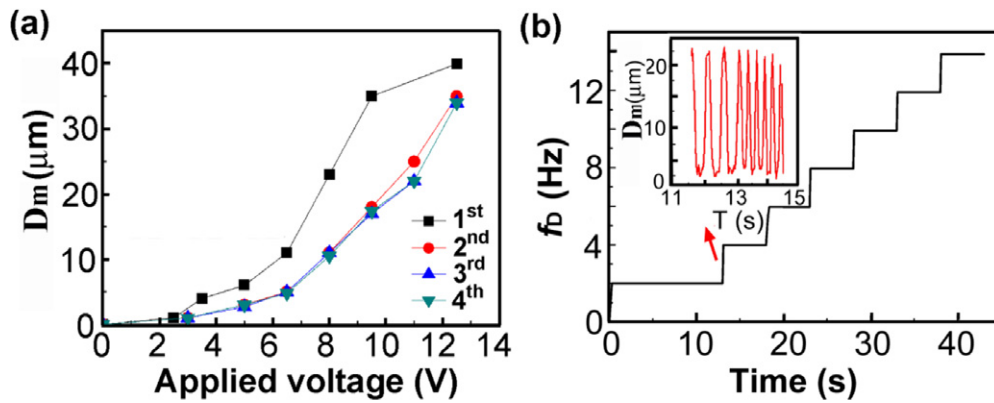


Figure 7. (a) The D_m profiles of device-A at various V and (b) the f_D - f profile. Inset: the time-evolved D_m profile at $f_D = 2 \rightarrow 4$ Hz ($t = 12$ s).

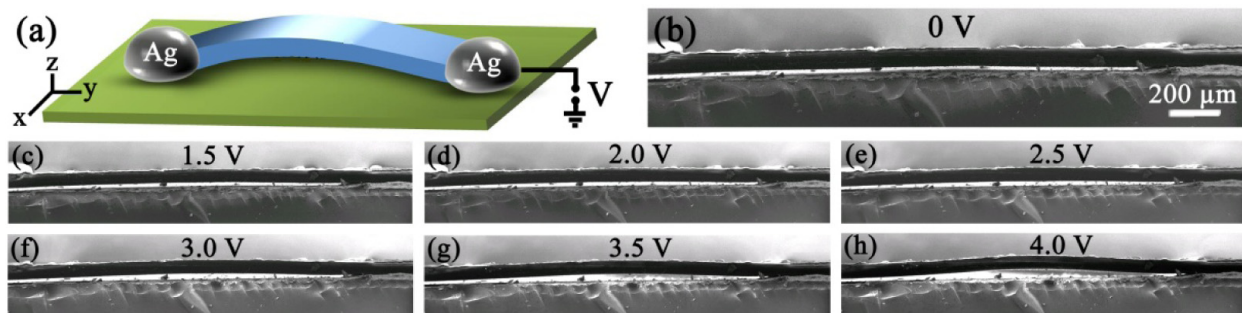


Figure 8. (a) A suspended beam made of dispersed MWCNTs and parylene at (b) 0 V, (c) 1.5 V, (d) 2 V, (e) 2.5 V, (f) 3 V, (g) 3.5 V, (h) 4 V.

interfaces, (ii) F_C creation between tubes, (iii) beam dilation along the y -axis and (v) beam deflection upon σ formation at beam ends. The F_C - σ driven actuations are verified as originating from CNT alignment, supported by high V_D , the linear plot of ε - V^2 , low joule heating and f_D - f synchronization.

Acknowledgment

We thank the National Science Council of Taiwan for financial support (NSC-99-2112-M-007-014-MY2).

References

- [1] Kane C L and Mele E J 1997 *Phys. Rev. Lett.* **78** 1932
- [2] Ding J J, Lu C L and Hsu W K 2011 *Appl. Phys. Lett.* **99** 033111
- [3] Baughman R H et al 1999 *Science* **284** 1340
- [4] Tahhan M, Truong V T, Spinks G M and Wallace G G 2003 *Smart Mater. Struct.* **12** 626
- [5] Foroughi J et al 2011 *Science* **334** 494
- [6] Lu S X and Panchapakesan B 2005 *Nanotechnology* **16** 2548
- [7] Hsu W K, Chu H Y, Chen T H, Cheng T W and Fang W L 2008 *Nanotechnology* **19** 135304
- [8] Lee S W, Lee D S, Morjan R E, Jhang S H, Sveningsson M, Nerushev O A, Park Y W and Campbell E E B 2004 *Nano Lett.* **4** 2027
- [9] Fan S S, Chapline M G, Franklin N R, Tomblor T W, Cassell A M and Dai H G 1999 *Science* **283** 512
- [10] Bonard J M, Salvetat J P, Stöckli T, Forró L and Châtelain A 1999 *Appl. Phys. A* **69** 245
- [11] Smith R C, Forrest R D, Carey J D, Hsu W K and Silva S R P 2005 *Appl. Phys. Lett.* **87** 013111
- [12] Lin Y H, Lai Y C, Hsu C T, Hu C J and Hsu W K 2011 *Phys. Chem. Chem. Phys.* **13** 7149
- [13] Fang W L, Chu H Y, Hsu W K, Cheng T W and Tai N H 2005 *Adv. Mater.* **17** 2987
- [14] Liu G T, Zhao Y C, Zheng K H, Liu Z, Ma W J, Ren Y, Xie S S and Sun L F 2009 *Nano Lett.* **9** 239
- [15] Last I, Levy Y and Jortner J 2002 *Proc. Natl Acad. Sci. USA* **99** 9107
- [16] Gao J, Yu A, Itkis M E, Bekyarova E, Zhao B, Niyogi S and Haddon R C 2004 *J. Am. Chem. Soc.* **126** 16698
- [17] Syue S H, Hsu C T, Chen U S, Chen H J, Hsu W K and Shih H C 2009 *Carbon* **47** 1239
- [18] Li L J, Zawadzka J and Uttamchandani D 2004 *J. Microelectromech. Syst.* **13** 83